Large eddy simulation study of turbulent kinetic energy and scalar variance budgets and turbulent/non-turbulent interface in planar jets

Tomoaki Watanabe[1]‡, **Yasuhiko Sakai**[2], **Koji Nagata**[1], **and Yasumasa Ito**[2]

[1]Department of Aerospace Engineering, Nagoya University, Nagoya, 464-8603, JAPAN

[2]Department of Mechanical Science and Engineering, Nagoya University, Nagoya, 464-8603, JAPAN

E-mail: watanabe.tomoaki@c.nagoya-u.jp

Abstract. Spatially developing planar jets with passive scalar transports are simulated for various Reynolds ($Re = 2,200$, $7,000$, and $22,000$) and Schmidt numbers ($Sc = 1$, 4, 16, 64, and 128) by the implicit large eddy simulation (ILES) using low-pass filtering as an implicit subgrid-scale model. The budgets of resolved turbulent kinetic energy k and scalar variance $\langle \phi'^2 \rangle$ are explicitly evaluated from the ILES data except for the dissipation terms, which are obtained from the balance in the transport equations. The budgets of k and $\langle \phi'^2 \rangle$ in the ILES agree well with the DNS and experiments for both high and low Re cases. The streamwise decay of the mean turbulent kinetic energy dissipation rate obeys the power low obtained by the scaling argument. The mechanical-to-scalar timescale ratio C_ϕ is evaluated in the self-similar region. For the high Re case, C_ϕ is close to the isotropic value ($C_\phi = 2$) near the jet centerline. However, when Re is not large, C_ϕ is smaller than 2 and depends on the Schmidt number. The T/NT interface is also investigated by using the scalar isosurface. The velocity and scalar fields near the interface depend on the interface orientation for all Re. The velocity toward the interface is observed near the interface facing in the streamwise, cross-streamwise, and spanwise directions in the planar jet in the resolved velocity field.

Keywords: Large Eddy Simulation, Jet, Mixing, Turbulent/non-turbulent Interface

‡ Corresponding author: watanabe.tomoaki@c.nagoya-u.jp

1. Introduction

Turbulent planar jets have been investigated over the year because they are simple examples of free shear flows, which can be seen in both engineering and environment. The fundamental characteristics of planar jets, such as self-similar profiles of statistics and flow structures, were revealed in many experiments by measuring velocity (e.g., Gutmark & Wygnanski 1976, Suresh et al. 2008, Deo et al. 2008). Passive scalar mixing in turbulent flows is also important in application, and in turbulent planar jets, it is often investigated by measuring concentration of dye or temperature (Su & Clemens 1999, Watanabe et al. 2012). Recently, miniaturized probes for velocity and pressure measurements have been developed and used in planar jets for investigating one point statistics of pressure (Terashima et al. 2012, 2014). Direct numerical simulation (DNS) is useful because three-dimensional data on all variables are available. Therefore, DNS is often applied to turbulent flows at moderate Reynolds numbers in a simple flow geometry. Spatially and temporally developing planar jets were investigated by using DNS in previous studies (e.g., Stanley et al. 2002, da Silva & Pereira 2008). However, because of the limitation of computational costs, the DNS of planar jets is limited to low Reynolds number cases.

Large eddy simulation (LES) is a useful tool for investigating turbulent flows with scalar transports at high Reynolds and Schmidt numbers, and it is expected to be applicable to engineering and environmental flows. LES can provide data on turbulent flows at high Reynolds and Schmidt numbers and flows in a complex geometry, which is difficult to obtain in experiments or DNS. LES resolves large-scale features in flows, whereas the effects of unresolved small-scale [subgrid scale (SGS)] fields have to be modeled. Various models have been proposed for modeling the SGS effects. Some of the SGS models are based on the eddy viscosity model (Smagorinsky 1963, Germano et al. 1991). When the eddy viscosity model is used for flow fields, the gradient diffusion model is often used for scalar fields with a dynamic procedure to determine the SGS turbulent Schmidt (Prandtl) number (Moin et al. 1991). One of the important characteristics in the SGS is energy or scalar dissipation, which has to be taken into account by SGS models. The eddy viscosity model and gradient diffusion model dissipate energy of velocity and scalar fluctuations by explicitly calculating the SGS terms in filtered governing equations (e.g., SGS Reynolds stress and SGS scalar flux). Recently, another approach for modeling the SGS effects is developed based on an artificial dissipation. In this approach, the dissipative feature in the SGS is emulated by a numerical dissipation without explicitly calculating the SGS terms. The LES using a numerical dissipation as an implicit SGS model is referred to as implicit LES (ILES) (Bogey & Bailly 2009). In the ILES, the dissipation in the SGS is often modeled by an explicit low-pass filter (Bogey & Bailly 2004). Mathew et al. (2003) developed the ILES based on a low-pass filter from the LES using the approximate deconvolution model (Stolz & Adams 1999). The ILES has been applied to various flows (Mathew et al. 2003, Bogey & Bailly 2006).

Free shear flows, such as jets and wakes, consist of turbulent and non-turbulent regions. These two regions are separated by an interfacial layer, which is called a turbulent/non-turbulent (T/NT) interface (da Silva et al. 2014). Recent studies show that the small-scale process near the interface plays an important role in the entrainment process (Westerweel et al. 2005). The eddy viscosity changes between turbulent and non-turbulent regions (da Silva 2009). Therefore, the SGS models based on the eddy viscosity are required to deal with the difference in the model parameter between the turbulent and non-turbulent regions. In the dynamic Smagorinsky model, the procedure to determine the model parameter often includes spatially averaging to prevent numerical instability (Le Ribault et al. 1999). Because of the difference in the model parameter between the turbulent and non-turbulent regions, this spatial average is not adequate for intermittent flows. Bogey & Bailly (2005) compared the LES results of sub-sonic round jets between the dynamic Smagorinsky model and the implicit model using numerical filtering, and showed that the eddy viscosity model reduces the effective Reynolds number and this reduction is not observed in the ILES. These studies on the LES indicate that the ILES is more useful for free shear flows than the classical LES based on the eddy viscosity.

In this study, planar jets with passive scalar transports are simulated for various Reynolds and Schmidt numbers by using the ILES. The ILES results are used for investigating the budget of turbulent kinetic energy and scalar variance in a self-similar region and large-scale characteristics of velocity and scalar fields near the T/NT interface. They were investigated in the DNS only for low Reynolds and Schmidt numbers. Although the turbulent kinetic energy budget was experimentally investigated in planar jets at a higher Reynolds number (Terashima et al. 2012, 2014), these experiments used some assumptions in evaluating the budget, such as local isotropy. In this study, we will provide detail data on turbulent kinetic energy and scalar variance budget for various Reynolds and Schmidt numbers. The Reynolds number and Schmidt number effects obtained in the LES are partial because of indirect effects on the resolved quantities through the SGS stress and scalar flux. We also investigate the characteristics of mean dissipation rates of turbulent kinetic energy and scalar variance in planar jets, and evaluate a mechanical-to-scalar timescale ratio, which is an important parameter in modeling turbulent reactive flows (Fox 2003). The T/NT interface was also investigated by the experiments by using particle image velocimetry and planar laser-induced fluorescence (Westerweel et al. 2009). However, it is worthwhile to compare the flow and scalar fields near the T/NT interface among different Reynolds numbers using LES. Previous studies using DNS showed that the interface characteristics are strongly affected by the interface orientations in planar jets (Watanabe et al. 2014*a*, 2014*b*). We also use the ILES results for investigating the effects of the interface orientation on the large-scale velocity and scalar fields near the interface. Section 2 describes the ILES of planar jets. In Sec. 3, we compare the self-similar characteristics among the ILES, DNS, and experiments for validating the ILES data, and then present the results relating to the budget of turbulent kinetic energy and scalar variance and the T/NT

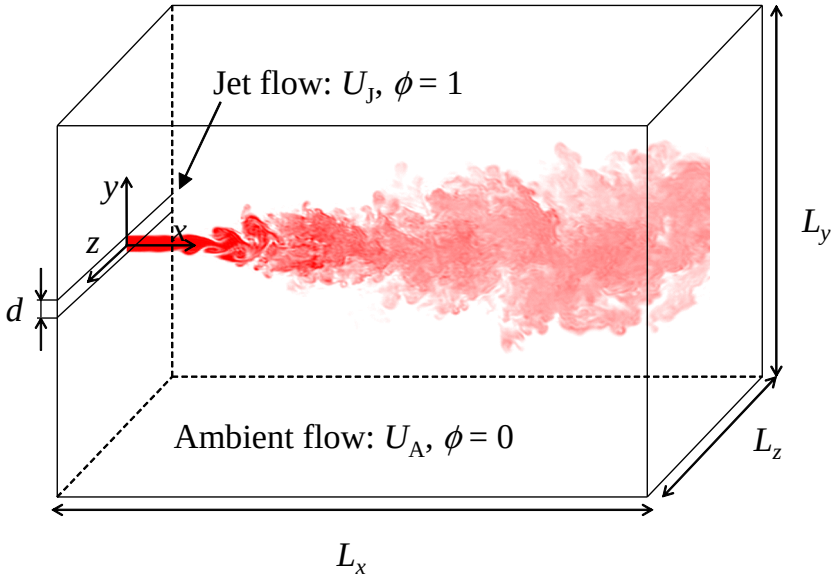

Figure 1. Turbulent planar jet with passive scalar transport.

interface. Finally, the conclusion is summarized in Sec. 4.

2. Implicit LES (ILES) of turbulent planar jet

2.1. Turbulent planar jets with passive scalar transport

The ILES is used for simulating spatially developing planar jets with a passive scalar ϕ (figure 1). The origin of the coordinate system is located at the center of the jet inlet. The streamwise, lateral, and spanwise directions are represented by x, y, and z, respectively. The ILES is performed for three Reynolds numbers $Re = U_J d/\nu = 2,200$, 7,000, and 22,000, where d is the width of the jet inlet, U_J is the mean bulk velocity at the jet inlet, and ν is the kinematic viscosity. The ILES for these Re is performed for passive scalars with five Schmidt numbers: $Sc = \nu/D = 1, 4, 16, 64$, and 128, where D is the molecular diffusivity for ϕ. At $x = 0$ in the ambient flow, the lateral and spanwise velocities are 0 and the streamwise velocity is $U_A = 0.056U_J$. The flow and scalar fields are periodic in the spanwise (z) direction. At $x = 0$ and the lateral boundaries, $\phi = 0$ and 1 are imposed in the ambient flow and jet inlet, respectively.

2.2. Implicit LES

We consider the continuity equation, Navier–Stokes equations, and transport equation for a passive scalar ϕ for an incompressible flow. The filtered governing equations used in the ILES are written as follows:

$$\frac{\partial \overline{U_j}}{\partial x_j} = 0, \tag{1}$$

$$\frac{\partial \overline{U_i}}{\partial t} + \frac{\partial \overline{U_j}\,\overline{U_i}}{\partial x_j} = -\frac{\partial \overline{P}}{\partial x_i} + \nu \frac{\partial^2 \overline{U_i}}{\partial x_j \partial x_j} + \mathcal{R}_i, \tag{2}$$

$$\frac{\partial \overline{\phi}}{\partial t} + \frac{\partial \overline{U_j}\,\overline{\phi}}{\partial x_j} = D \frac{\partial^2 \overline{\phi}}{\partial x_j \partial x_j} + \mathcal{R}_\phi, \tag{3}$$

where U_i is the instantaneous velocity and P is the instantaneous pressure divided by the density. The overbar denotes the low-pass filtered quantity. The SGS terms ($\mathcal{R}_i$ and $\mathcal{R}_\phi$) appear in the filtered Navier–Stokes equations and filtered scalar transport equation, and are often modeled using the eddy viscosity model for $\mathcal{R}_i$ and the gradient diffusion model for $\mathcal{R}_\phi$. In the ILES in this study, a low-pass filter, which damps small-scale energy without affecting large-scales, is used for emulating the dissipation in the SGS instead of the explicit computation of $\mathcal{R}_i$ and $\mathcal{R}_\phi$. For this purpose, we use the composite filter $(Q_N * G)$, where G is the explicit low-pass filter with a five-point stencil proposed by Stolz et al. (2001*a*) and $Q_N \approx G^{-1}$ is the approximate deconvolution filter of G computed by the van Cittert deconvolution method (Stolz & Adams 1999):

$$Q_N = \sum_{n=0}^{N} (I - G)^n. \tag{4}$$

Here, I is the identity operator. The approximate deconvolution filter Q_N can be obtained by truncating the expanded series at N in equation. (4). We set $N = 5$ as in the LES using the approximate deconvolution model (Stolz et al. 2001*b*). For the low-pass filter G, the composite filter $(Q_N * G)$ becomes the low-pass filter whose cut-off lengthscale is slightly smaller than that of G (Mathew et al. 2003). Thus, $(Q_N * G)$ has smaller effects on large-scales than the original filter G, but can damp the small-scale fluctuations. The low-pass filter $(Q_N * G)$ is applied to the velocity and scalar every three computational time steps.

The ILES code is developed from the DNS code based on a finite difference method used in previous studies (Watanabe et al. 2014*c*, 2014*d*). The fully conservative fourth-order central difference scheme (Morinishi et al. 1998) is used for spatial discretization in the x and z directions, and the fully conservative second-order central difference scheme is used in the y direction. Equations (1) and (2) are solved using the fractional step method. The Poisson equation is solved by the fast Fourier transform (in the spanwise direction), the cosine transform (in the streamwise direction), and a tridiagonal matrix algorithm (in the lateral direction). The Crank–Nicolson method is used for the time integration of the y directional viscous and molecular diffusion terms, whereas the third-order Runge–Kutta method is used for the other terms (Spalart et al. 1991). The computational time step is set to $dt = 0.032d/U_\mathrm{J}$.

For confirming the ILES results are independent of the computational grid size, the ILES is performed for two different sizes of the computational domain with the number of the computational grid points $N_x \times N_y \times N_z = 512 \times 280 \times 32$. The computational domain sizes in the two ILES are $L_x \times L_y \times L_z = 14.5\pi d \times 11.0\pi d \times 2.2\pi d$ in the coarse-grid ILES and $11.0\pi d \times 8.0\pi d \times 1.8\pi d$ in the fine-grid ILES. The grid size in the coarse-grid ILES is about 1.3 times larger than that in the fine-grid ILES. The effects of

the low-pass filter used in the ILES depend on the grid size. In this paper, the fine-grid ILES is used for investigating the grid-size dependence of the ILES results. The uniform grid is used in the x and z directions. In the y direction, a fine grid is used near the jet centerline, and the grid is stretched near the lateral boundaries. The periodic boundary conditions are applied in the spanwise direction. The slip conditions are applied at the lateral boundaries. The convective boundary condition with viscous and molecular diffusion terms (Dai et al. 1994) is used for $\overline{U_i}$ and $\overline{\phi}$ at the outlet plane. The velocity at the jet inlet ($x = 0$) is generated by superimposing velocity fluctuations on the mean velocity. The fluctuating components of the inflow velocity are generated by a diffusion process that converts the random noise into the fluctuations which possess the required length scales (Kempf et al. 2005). The characteristics length scales of the velocity fluctuations are set to $0.29d$ at the jet inlet. The profiles of mean and rms velocities at the jet inlet are the same as in previous DNS (Watanabe et al. 2014*c*, 2014*d*), and are similar to the inflow velocity measured in the experimental apparatus (Watanabe et al. 2012, 2014*e*). At the center of the jet inlet, the rms streamwise velocity fluctuation is $2.3\times10^{-3}U_\mathrm{J}$. The turbulent Reynolds numbers based on the Taylor microscale calculated from the streamwise velocity are 1.1, 3.6, and 11.2 for $Re = 2,200$, $7,000$, and $22,000$, respectively.

At $(x, y) = (40d, 0)$ in the coarse-grid ILES, the integral lengthscale L_U is $2.4d$ for the case $Re = 22,000$, where L_U is calculated from the auto-correlation function of the streamwise velocity according to Deo et al. (2013). This integral lengthscale at $x = 40d$ is close to the value obtained by the extrapolation of the experimental data (Deo et al. 2013). At this streamwise location, the domain size in the z direction, L_z, is 2.9 times larger than the integral lengthscale. The integral lengthscale increases in the downstream direction. Most results in this paper are presented for the upstream region where L_z is larger than $3L_U$. The spanwise length of the computational domain in the present ILES is larger than the previous DNS and LES of planar jets (Watanabe et al. 2014*c*, da Silva et al. 2015). Even in the simulations with the smaller computational domain, the development of large-scale characteristics, such as mean velocity and jet width, are consistent with experimental measurements.

3. Results and Discussion

3.1. Self-similar Characteristics of Turbulent Planar Jet

We examine the self-similar characteristics of the planar jet. The DNS was conducted by authors for the planar jet at $Re = 2,200$ and $Sc = 1$ and 4 in a small computational domain (Watanabe et al. 2014*c*, 2014*d*). The numerical methods and inflow boundary conditions used in the DNS are similar to the present ILES. The planar jet at $Re = 2,200$ investigated in the ILES is also similar to the experiments of a planar liquid jet, in which streamwise and lateral velocities and concentration of dye ($Sc \approx 600$) have been measured (Watanabe et al. 2014*e*). Therefore, the statistics are compared among the

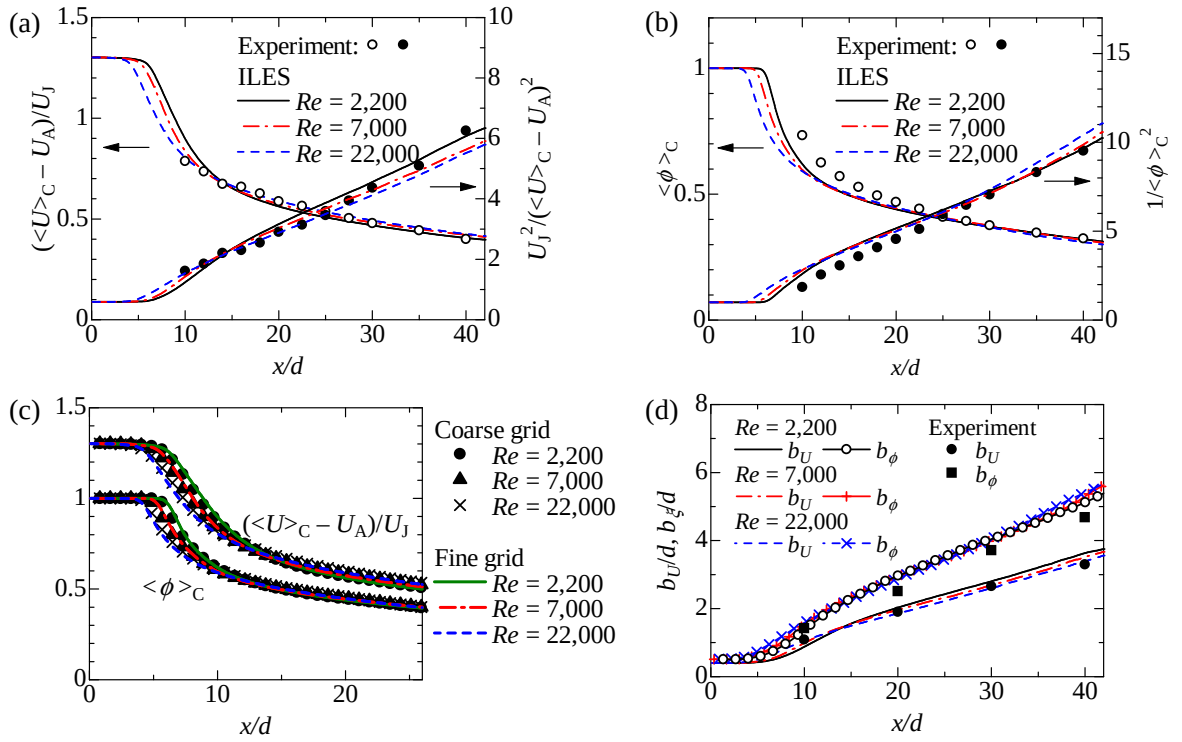

Figure 2. Characteristics of mean streamwise velocity and mean scalar profiles. Streamwise evolutions of (a) mean streamwise velocity $\langle U\rangle_{\mathrm{C}}$ and (b) mean scalar $\langle\phi\rangle_{\mathrm{C}}$ on the jet centerline. The ILES results are compared with the experiment (Watanabe et al. 2014*e*) ($Re = 2,200$, $Sc \approx 600$). (c) The dependence of $\langle U\rangle_{\mathrm{C}}$ and $\langle\phi\rangle_{\mathrm{C}}$ on the spatial resolution of the ILES. (d) Streamwise evolutions of jet half-width based on mean streamwise velocity and mean scalar. The ILES results are compared with the experiment (Watanabe et al. 2014*e*) ($Re = 2,200$, $Sc \approx 600$).

ILES, DNS, and experiments.

Figures 2(a) and (b) show the mean streamwise velocity $\langle U\rangle_{\mathrm{C}}$ and mean scalar $\langle\phi\rangle_{\mathrm{C}}$ for $Sc = 1$ on the jet centerline ($y = 0$), respectively. Here, $\langle\ \rangle$ denotes a mean value, and the subscript C refers to the value on the jet centerline. In the ILES, the statistics are calculated from resolved fields, such as $\overline{U_i}$ and $\overline{\phi}$. For example, $\langle f\rangle$ is estimated by taking time-average of $\overline{f}$. Because we confirmed that the Schmidt number hardly affects the mean scalar field, $\langle\phi\rangle_{\mathrm{C}}$ is shown for $Sc = 1$. The streamwise evolutions agree well with the experimental results, and $\langle U\rangle_{\mathrm{C}} - U_{\mathrm{A}}$ and $\langle\phi\rangle_{\mathrm{C}}$ decrease with proportion to $(x/d)^{-0.5}$. In the ILES of the jets at three Re, the potential-core length, which is the streamwise length of constant $\langle U\rangle_{\mathrm{C}}$ and $\langle\phi\rangle_{\mathrm{C}}$, decreases with increasing Re, in agreement with previous DNS (Wu et al. 2014) and experiments (Suresh et al. 2008, Deo et al. 2008). Figure 2(c) compares $\langle U\rangle_{\mathrm{C}}$ and $\langle\phi\rangle_{\mathrm{C}}$ between the fine-grid and coarse-grid ILES. In both simulations, we can find that the potential-core length is shorter for higher Re.

Figure 2(d) shows the jet half-width (b_U and b_ϕ) based on $\langle U\rangle - U_{\mathrm{A}}$ and $\langle\phi\rangle$ for $Sc = 1$. The jet half-width increases with proportion to x/d, and the ILES results are

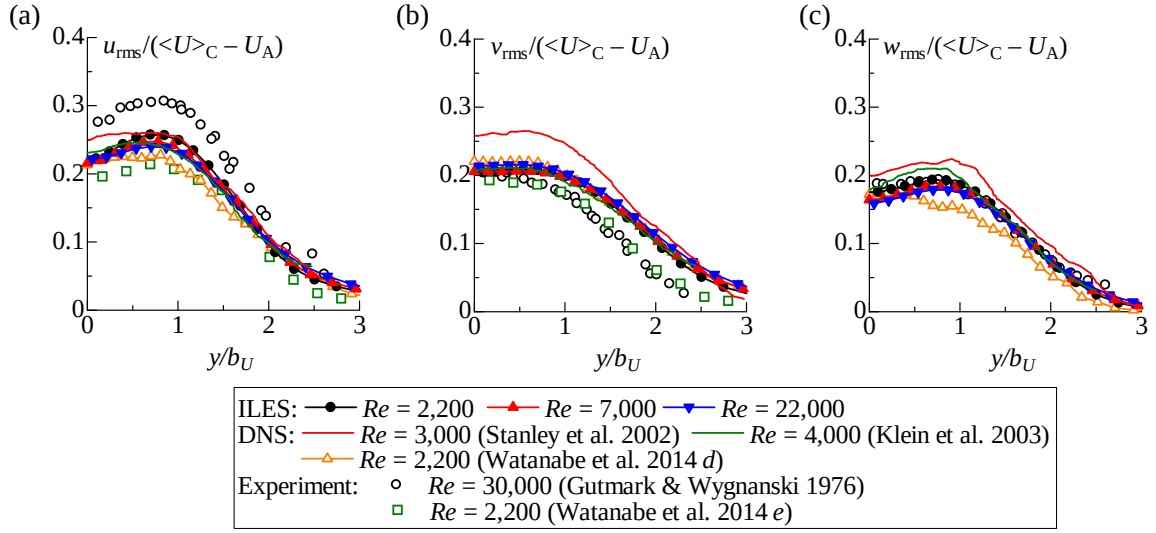

Figure 3. Lateral profiles of rms velocity normalized by $(\langle U\rangle_C - U_A)$: (a) streamwise rms velocity; (b) lateral rms velocity; (c) spanwise rms velocity. The ILES results at $x/d = 25$ are shown. The results are compared with the DNS by Stanley et al. (2002) ($Re = 3,000$), Klein et al. (2003) ($Re = 4,000$), and Watanabe et al. (2014*d*) ($Re = 2,200$) and the experiments by Gutmark & Wygnanski (1976) ($Re = 30,000$) and Watanabe et al. (2014*e*) ($Re = 2,200$).

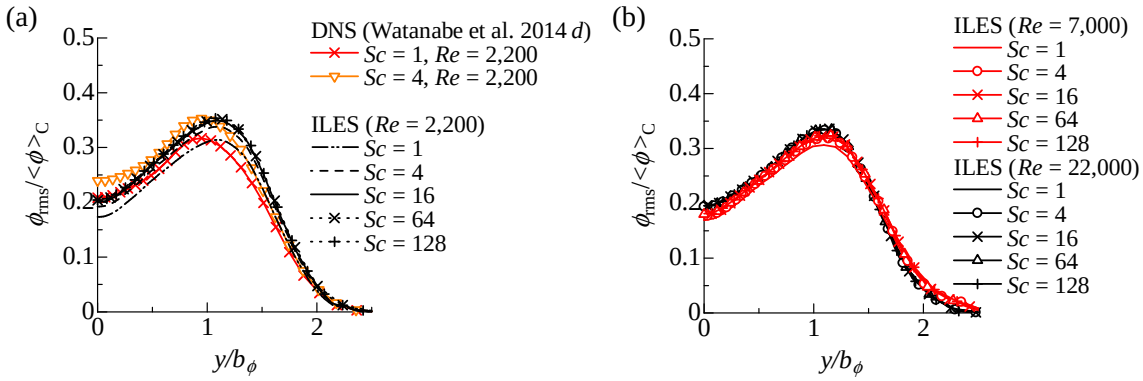

Figure 4. Lateral profiles of rms scalar ϕ_{rms} normalized by $\langle\phi\rangle_C$ at $x/d = 25$: (a) $Re = 2,200$; (b) $Re = 7,000$ and $22,000$. In (a), the ILES results are compared with the DNS by Watanabe et al. (2014*d*) ($Re = 2,200$, $Sc = 1$ and 4).

very similar to the experiments (Watanabe et al. 2014*e*). It is found that the spreading rate of mean velocity is almost independent of Re, and by applying the least-squared method to b_U for $x/d > 20$, we can obtain $db_U/dx = 0.078$ for all Re. The spreading rate of $\langle\phi\rangle$ slightly increases with increasing Re, and the least-squared method yields $db_\phi/dx = 0.11$, 0.12, and 0.13 for $x/d > 20$ in the planar jets at $Re = 2,200$, $7,000$, and $22,000$, respectively.

Figure 3 compares the self-similar profiles of rms velocity among the ILES, DNS,

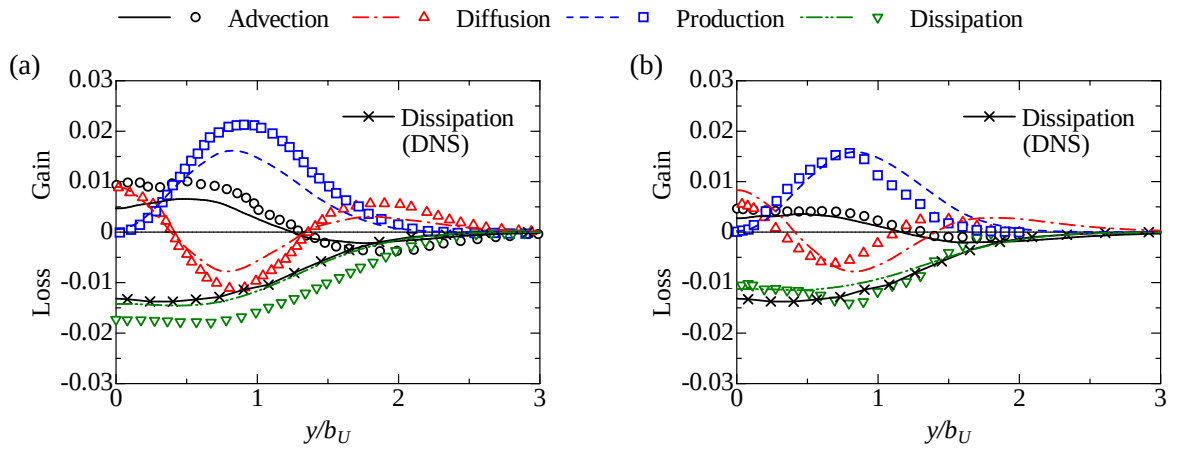

Figure 5. Budget of turbulent kinetic energy normalized by $(\langle U\rangle_{\rm C} - U_{\rm A})^3/b_U$ at $x/d = 30$: (a) $Re = 2,200$; (b) $Re = 22,000$. The ILES results (lines) in (a) and (b) are compared with the DNS by Stanley et al. (2002) ($Re = 3,000$) and the experiment by Terashima et al. (2014) ($Re = 22,000$), respectively. The profiles obtained by Stanley et al. (2002) and Terashima et al. (2014) are shown by symbols. The dissipation term in the planar jet at $x/d = 30$ obtained by the DNS (Watanabe et al. 2014*a*) ($Re = 2,200$) is also shown.

and experiments. The rms velocity profiles are slightly different among previous experiments and DNS, which might be caused by differences in the inflow velocity at the jet inlet. However, a similar trend is found in all experiments and DNS. It is found that the self-similar profiles in the ILES are also similar to the DNS and experimental results. The self-similar profiles of the rms velocity are almost independent of Re in the present ILES, where the planar jets at different Reynolds numbers are computed for the same inflow condition. Figure 4 shows the rms scalar ($\phi_{\rm rms}$) normalized by $\langle\phi\rangle_{\rm C}$. The DNS results for $Re = 2,200$ and $Sc = 1$ and 4 are also shown in figure 4(a). In both ILES and DNS, $\phi_{\rm rms}$ increases with increasing Sc at $Re = 2,200$ although the Sc dependence is small for $Sc > 16$. However, for the high Re cases shown in figure 4(b), $\phi_{\rm rms}$ hardly changes with Sc. These results presented above show that the planar jets computed by the ILES have self-similar characteristics similar to the previous DNS and experimental results.

3.2. Budget of turbulent kinetic energy and scalar variance

We investigate the budget of the resolved turbulent kinetic energy $k \equiv (\langle u^2\rangle + \langle v^2\rangle + \langle w^2\rangle)/2$ and the resolved scalar variance $\langle\phi'^2\rangle$ in the self-similar region, where $u_i \equiv \overline{U_i} - \langle\overline{U_i}\rangle$ and $\phi' \equiv \overline{\phi} - \langle\overline{\phi}\rangle$ are the resolved velocity and scalar fluctuations, respectively. The transport equation of k is given by

$$\frac{\partial k}{\partial t} = \underbrace{-\langle\overline{U_j}\rangle\frac{\partial k}{\partial x_j}}_{\rm I} \underbrace{-\frac{1}{2}\frac{\partial\langle u_j u_j u_i\rangle}{\partial x_i}}_{\rm II} \underbrace{-\frac{\partial\langle u_j p\rangle}{\partial x_j}}_{\rm III} \underbrace{+\nu\frac{\partial^2 k}{\partial x_j\partial x_j}}_{\rm IV} \underbrace{-\langle u_i u_j\rangle\frac{\partial\langle\overline{U_i}\rangle}{\partial x_j}}_{\rm V} \underbrace{-\epsilon}_{\rm VI}. \quad (5)$$

where I is the advection term by a mean flow, II the turbulent diffusion term, III the pressure diffusion term, IV the viscous diffusion term, V the production term, and VI the dissipation term ($p = \overline{P} - \langle \overline{P} \rangle$: resolved fluctuating pressure). Although the dissipation in equation (5) is contributed by the resolved fields and the numerical scheme, such as a low-pass filter (Bogey & Bailly 2009), we use only the total dissipation, which is the sum of the dissipations in the resolved scales and by the low-pass filter. We simply refer the sum of terms II, III, and IV as the diffusion terms. In the planar jet, $\partial k/\partial t = 0$. Therefore, as in Bogey & Bailly (2006), the right-hand side except for ϵ is explicitly evaluated from the resolved field of the ILES, and then ϵ is calculated from the balance. Figure 5 shows the lateral profiles of equation (5) normalized by $(\langle U \rangle_{\mathrm{C}} - U_{\mathrm{A}})^3/b_U$. The turbulent kinetic energy equation obtained by the DNS (Stanley et al. 2002, Watanabe et al. 2014*a*) and experiment (Terashima et al. 2014) are also shown for comparison. The budget of k estimated by the ILES qualitatively agrees well with the DNS and experiment for both Re. The Re dependence of the budget of k is small. The turbulent kinetic energy generated by the production term around $y/b_U = 1$ is transferred toward the jet centerline and the outer region by the diffusion terms. Figures 6(a) and (b) show the turbulent diffusion and pressure diffusion terms (II and III), respectively. In the planar jet investigated in this study, the viscous diffusion term is small and negligible. The ILES results are similar to the experiments by Terashima et al. (2014) although positive and negative peaks in the turbulent diffusion term appear at different locations. It is found that the pressure diffusion term is relatively small compared with the turbulent diffusion term, but is not negligible in the planar jet. The difference in figure 6(a) between the experiment and the ILES might be explained by the different inflow conditions. In the experiment by Terashima et al. (2014), the mean velocity at the jet inlet is expected to exhibit a tophat profile because the nozzle attachment which takes out the boundary layers inside the jet nozzle is installed. The mean inflow velocity in the ILES is determined according to the experiments (Watanabe et al. 2012), in which no nozzle attachments are used and the boundary layers are developed near the wall inside the nozzle as confirmed in the mean velocity at the jet inlet shown by Watanabe et al. (2014*d*). The difference in the mean velocity profile at the jet inlet greatly affects the jet development (Wu et al. 2013).

The transport equation of resolved scalar variance $\langle \phi'^2 \rangle$ is written as follows:

$$\frac{\partial \langle \phi'^2 \rangle}{\partial t} = \underbrace{-\langle \overline{U_j} \rangle \frac{\partial \langle \phi'^2 \rangle}{\partial x_j}}_{\mathrm{I}} \underbrace{-\frac{\partial \langle u_j \phi'^2 \rangle}{\partial x_j}}_{\mathrm{II}} \underbrace{+D \frac{\partial^2 \langle \phi'^2 \rangle}{\partial x_j \partial x_j}}_{\mathrm{III}} \underbrace{-2 \langle u_j \phi' \rangle \frac{\partial \langle \overline{\phi} \rangle}{\partial x_j}}_{\mathrm{IV}} \underbrace{-\epsilon_\phi}_{\mathrm{V}}, \tag{6}$$

where I is the advection term by a mean flow, II the turbulent diffusion term, III the molecular diffusion term, IV the production term, and V the dissipation term, which includes the contributions by the resolved field and low-pass filtering. Similar to equation (5), the mean scalar dissipation rate of resolved scalar variance, ϵ_ϕ, is obtained from the balance in equation (6), and the other terms are explicitly evaluated from the ILES data. Figure 7 shows the lateral profiles of each term in equation (6) normalized by $(\langle U \rangle_{\mathrm{C}} - U_{\mathrm{A}}) \langle \phi \rangle_{\mathrm{C}}^2 / b_\phi$ for $Sc = 1$ at $Re = 2,200$ and $22,000$. Because we confirmed

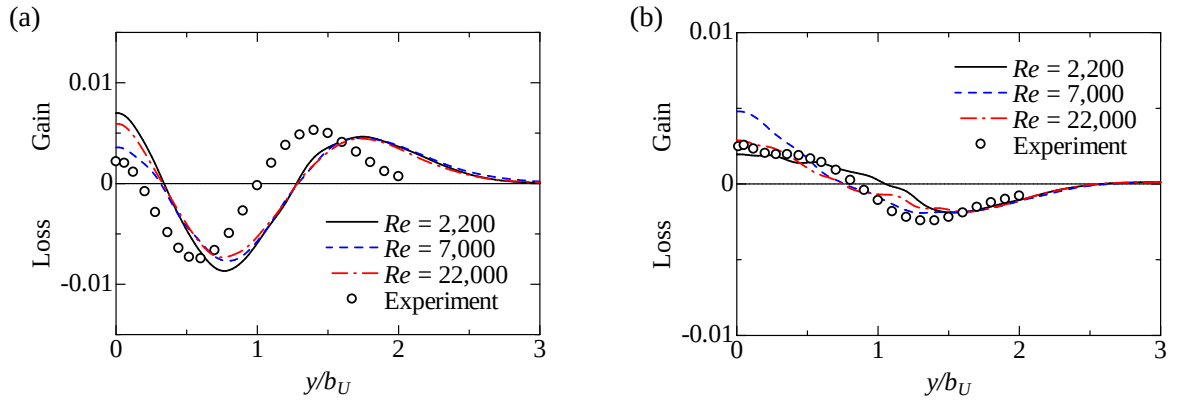

Figure 6. Lateral profiles of diffusion terms normalized by $(\langle U\rangle_{\rm C} - U_{\rm A})^3/b_U$ at $x/d = 30$: (a) turbulent diffusion term (Ⅱ); (b) pressure diffusion term (Ⅲ) in equation (5). The ILES results (lines) at $x/d = 30$ are compared with the experiment by Terashima et al. (2014) ($Re = 22,000$)

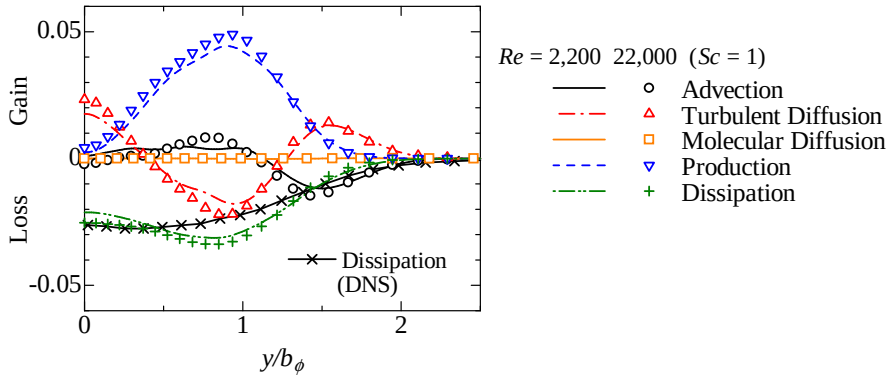

Figure 7. Budget for scalar variance for $Sc = 1$ normalized by $(\langle U\rangle_{\rm C} - U_{\rm A})\langle\phi\rangle_{\rm C}^2/b_U$ at $x/d = 30$ for $Re = 2,200$ (lines) and $22,000$ (symbols). The dissipation term in the planar jet at $x/d = 30$ obtained by the DNS (Watanabe et al. 2014*a*) ($Re = 2,200$ and $Sc = 1$) is also shown.

that the budget of $\langle\phi'^2\rangle$ is almost independent of Sc, we only show the results for $Sc = 1$. For comparison, the dissipation rate of scalar variance explicitly calculated in the DNS (Watanabe et al. 2014*a*) is also shown in this figure. The profiles hardly change with Re, and only the molecular diffusion term is negligible. Although the dissipation term obtained by the ILES has a negative peak at $|y/b_\phi| \approx 0.8$, this peak does not appear in the DNS result. However, the difference in ϵ_ϕ is not large between the ILES and the DNS.

Figure 8(a) shows the streamwise decay of ϵ on the jet centerline. At high Re, ϵ is expected to be equal to the supply rate of k from the large-scale fields (Deo et al. 2008). Then, ϵ is of the order of $(\langle U\rangle_{\rm C} - U_{\rm A})^3/b_U$. Because $(\langle U\rangle_{\rm C} - U_{\rm A}) \sim (x/d)^{-0.5}$ and $b_U \sim (x/d)$ as in figures 2(a) and (d), $\epsilon d/(U_{\rm J} - U_{\rm A})^3 = K_\epsilon (x/d)^{-2.5}$ in the self-similar region on the jet centerline (Deo et al. 2008), where K_ϵ is influenced by nozzle conditions

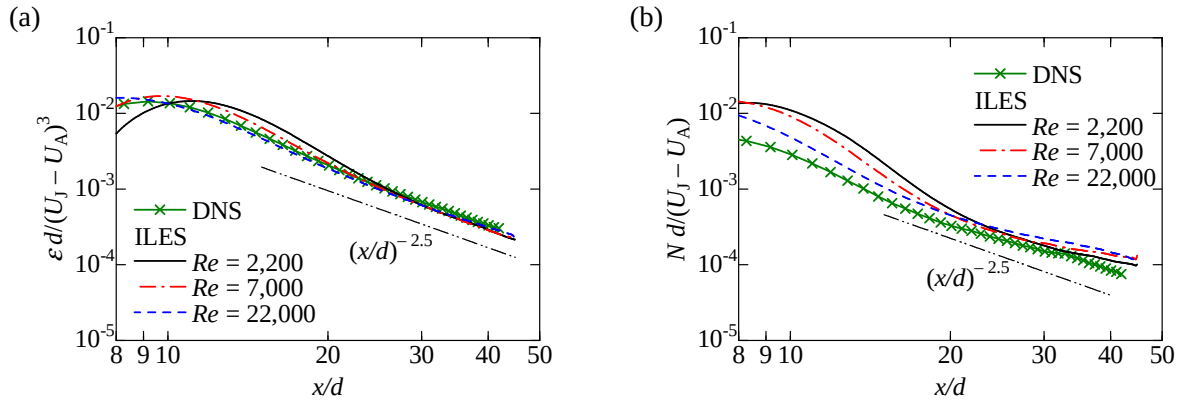

Figure 8. Streamwise evolutions of (a) mean turbulent kinetic energy dissipation rate ϵ and (b) mean scalar dissipation rate N for $Sc = 1$ in the ILES and DNS (Watanabe et al. 2014*a*) ($Re = 2,200$ and $Sc = 1$).

(Deo et al. 2013). In figure 8(a), we can find that ϵ decays with proportion to $(x/d)^{-2.5}$ in the downstream region. In the ILES results, the region in which $\epsilon \sim (x/d)^{-2.5}$ holds is extended to the upstream region for the high Re cases. Although ϵ strongly depends on Re in the upstream region, this Re dependence becomes small in the self-similar region. The least-square method for ϵ in the region of $x/d > 20$ yields $K_\epsilon = 3.4$ for $Re = 22,000$, which is larger than $K_\epsilon = 0.9 \sim 2.2$ in the experiments of planar jets (Deo et al. 2008).

For the mean scalar dissipation rate $N \equiv \epsilon_\phi/2$, Bilger (2004) obtained $N \sim (x/d)^{-2.5}$ on the center of the planar jet from the transport equation for ϕ^2 under the assumption of the self-similarity. Figure 8(b) shows the streamwise decay of N for $Sc = 1$ on the jet centerline. In the downstream region, the decay rate of N obtained by the ILES and DNS is smaller than -2.5. Su & Clemens (1999) measured the scalar dissipation rate in a planar jet, and their measurement also shows $N \sim (x/d)^{-1.4}$, for which the decay rate is smaller than -2.5. In the present ILES data, $N \sim (x/d)^{-1.6}$ and $\sim (x/d)^{-1.5}$ are obtained in the region of $x/d > 25$ for $Re = 2,200$ and $22,000$, respectively, and are close to the experimental results (Su & Clemens 1999) rather than the theoretical prediction.

In some of numerical methods for turbulent reactive flows, such as probability density function (PDF) methods (Pope 1985), the mean scalar dissipation rate has to be modeled. The most widely used model is the equilibrium model (Fox 2003):

$$\epsilon_\phi = C_\phi \frac{\epsilon}{k} \langle \phi'^2 \rangle, \tag{7}$$

where $C_\phi = 2\tau/\tau_\phi$ is the mechanical-to-scalar timescale ratio, which is the ratio of the turbulence timescale $\tau \equiv k/\epsilon$ to the scalar mixing timescale $\tau_\phi \equiv 2\langle \phi'^2 \rangle/\epsilon_\phi$ (Corrsin 1951). C_ϕ is treated as a model parameter. In isotropic turbulence at high Re and Sc, $C_\phi = 2$ (Schwertfirm & Manhart 2007). However, various values of C_ϕ have been used in numerical simulations (Lindstedt et al. 2000, Xu & Pope 2000, Mitarai

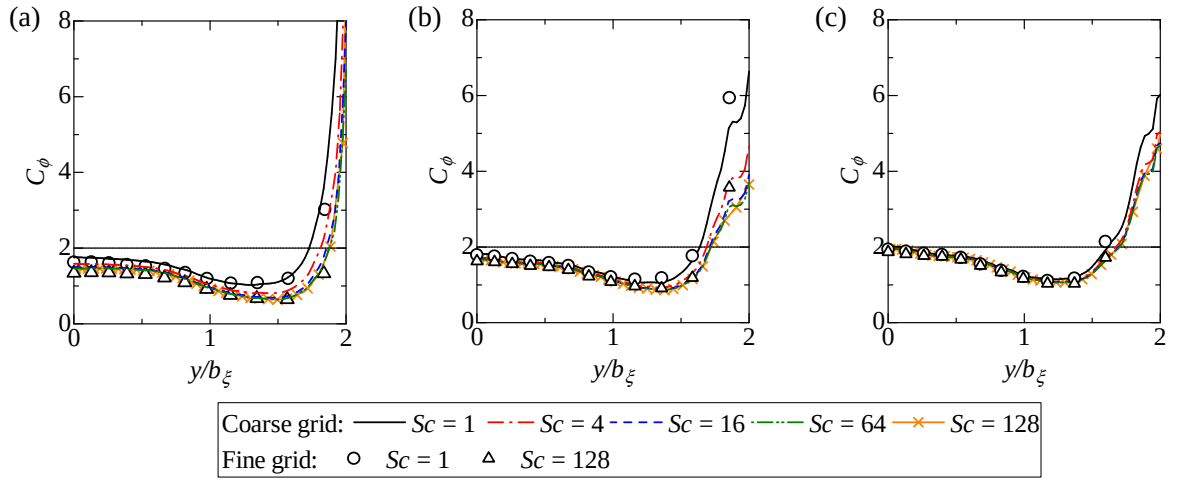

Figure 9. Lateral profiles of mechanical-to-scalar timescale ratio $C_\phi = 2\tau/\tau_\phi$ at $x/d = 30$: (a) $Re = 2,200$; (b) $Re = 7,000$; (c) $Re = 22,000$. The lateral solid line shows $C_\phi = 2$, which is the value in isotropic turbulence at high Reynolds number. C_ϕ for $Sc = 1$ and 128 obtained by the fine-grid ILES is also shown for comparison.

et al. 2005). We evaluate C_ϕ in the planar jets by using ϵ and ϵ_ϕ obtained from equations (5) and (6) in the ILES, and the results are shown in figure 9 for the various Re and Sc. For comparison, the fine-grid ILES results for $Sc = 1$ and 128 are also shown in the figures. For all cases, C_ϕ decreases in the y direction from $y = 0$, and then rapidly increases from $|y/b_\phi| \approx 1.5$. Note that both turbulent and non-turbulent fluids intermittently appear in the region of $|y/b_\phi| > 1$ (Watanabe et al. 2014*b*). Therefore, the flow is far from isotropy in this region. The isotropic value $C_\phi = 2$ is observed only near the jet centerline for $Re = 22,000$. Except for the outer region ($|y/b_\phi| > 1.5$), C_ϕ for $Sc = 1$ ranges from 1.0 to 1.8 for $Re = 2,200$ and from 1.2 to 2.0 for $Re = 22,000$. For $Re = 2,200$ and $7,000$, C_ϕ is slightly smaller than 2 even near the jet centerline. Near the jet centerline, C_ϕ for the small Re cases decreases as Sc increases. A similar Sc dependence of C_ϕ was found in a turbulent channel flow (Schwertfirm & Manhart 2007). However, C_ϕ does not depend on Sc except for the outer region when Re is large as in figure 9(c). These Re and Sc dependence of C_ϕ can be seen in both fine-grid and coarse-grid ILES.

3.3. Large-scale characteristics of velocity and scalar fields near the T/NT interface

Here, we investigate the velocity and scalar fields near the T/NT interface. Because the small-scale fields are not resolved in the ILES, we focus only on the large-scale characteristics. In previous DNS studies (Bisset et al. 2002, da Silva & Pereira 2008), the T/NT interface is detected with the isosurface of vorticity magnitude. In the present ILES, the T/NT interface is detected with the isosurface of ϕ for $Sc = 1$ because the scalar interface detected as the scalar isosurface is quite similar to the isosurface of vorticity magnitude for $Sc = 1$ (Gampert et al. 2014*a*). Gampert et al. (2014*b*) also

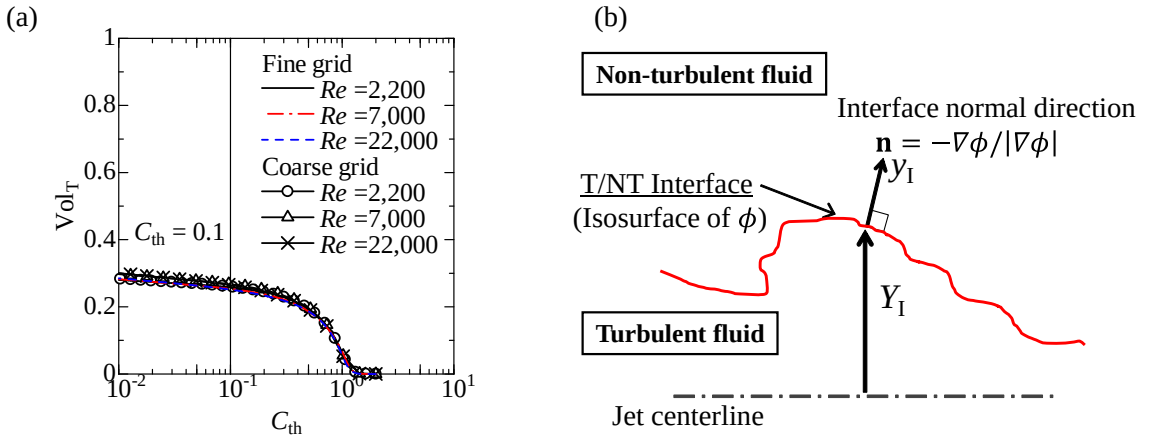

Figure 10. Detection of T/NT interface by thresholding passive scalar. (a) Volume fraction of turbulent region in the region of $11.4 \leq x/d \leq 34.1$ ($8.8 \leq x/d \leq 25.9$) as a function of the threshold $C_{\rm th}$ calculated in the coarse-grid (fine-grid) ILES. (b) Definition of local coordinate $y_{\rm I}$ used for calculating conditional statistics conditioned on the distance from the T/NT interface. The interface height $Y_{\rm I}$ is also shown in this figure.

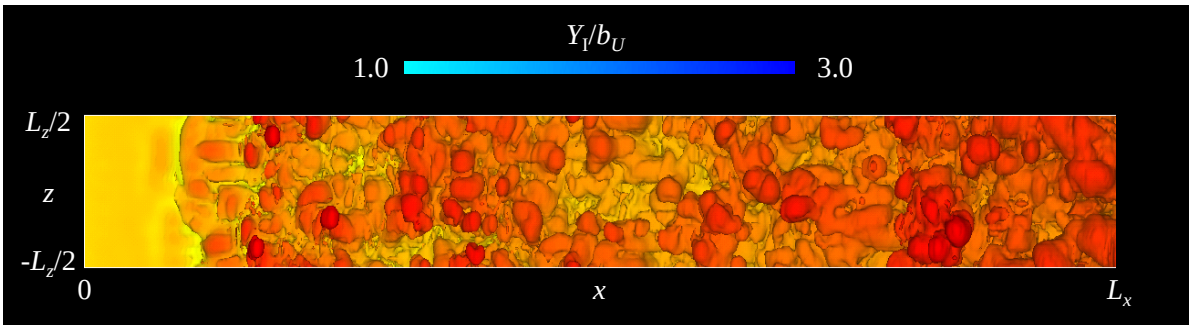

Figure 11. Visualization of T/NT interface (scalar isosurface) in planar jet at $Re = 7,000$. The color of the interface shows the interface height $Y_{\rm I}$ from the jet centerline.

used the scalar isosurface for investigating the T/NT interface in the LES. The turbulent region is defined as the region of $\phi/\langle\phi\rangle_{\rm C} \geq C_{\rm th}$ for $Sc = 1$, and the interface is detected with the isosurface of $\phi/\langle\phi\rangle_{\rm C} = C_{\rm th}$, where $C_{\rm th}$ is the interface detection threshold. As in Taveira et al. (2013), the threshold is determined from the dependence of the turbulent volume on $C_{\rm th}$. Figure 10(a) shows the volume fraction of the turbulent region, $\mathrm{Vol_T}$, as a function of $C_{\rm th}$. Although $\mathrm{Vol_T}$ increases as $C_{\rm th}$ decreases, $\mathrm{Vol_T}$ slowly changes with the threshold for $C_{\rm th} < 0.2$. The relationship between $\mathrm{Vol_T}$ and $C_{\rm th}$ is almost the same for both fine-grid and coarse-grid ILES. In this study, we use $C_{\rm th} = 0.1$.

Conditional statistics are calculated conditioned on the distance from the interface (Bisset et al. 2002). The distance from the interface, $y_{\rm I}$, is defined as in figure 10(b). In this figure, the interface height $Y_{\rm I}$ is also defined. The normal direction of the

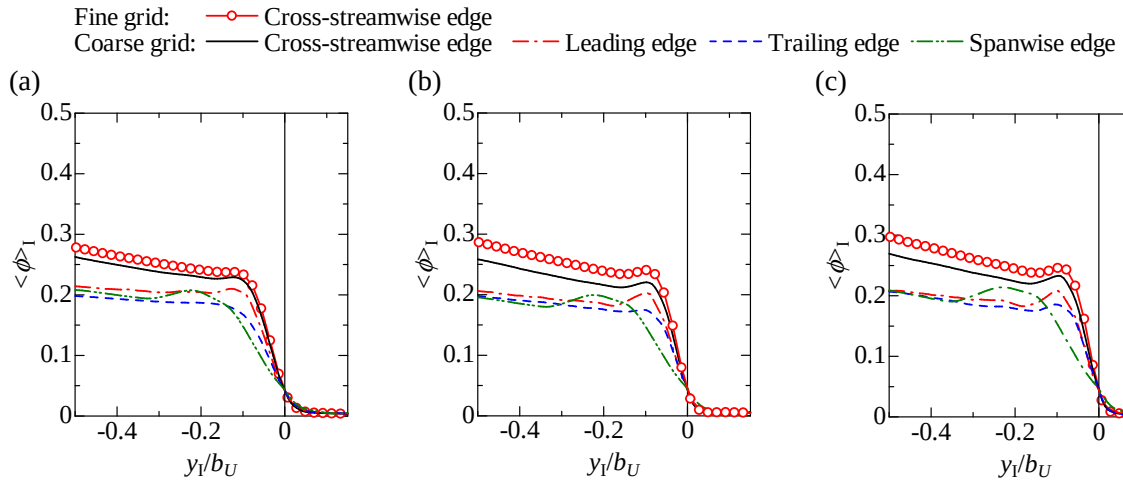

Figure 12. Conditional mean scalar near cross-streamwise, leading, trailing, and spanwise edges at $x/d = 23$ obtained by the coarse-grid ILES: (a) $Re = 2,200$; (b) $Re = 7,000$; (c) $Re = 22,000$. For the cross-streamwise edge, the conditional profiles obtained by the fine-grid ILES are also shown for comparison.

scalar isosurface is given by the unit normal vector $\mathbf{n} = (n_x, n_y, n_z) = -\nabla\phi/|\nabla\phi|$. The conditional statistics are calculated by using the same procedure as in previous studies (Watanabe et al. 2014*c*, 2014*d*). The conditional mean value is denoted by $\langle\ \rangle_{\rm I}$. The conditional statistics are calculated separately for four interface orientations, which are called the cross-streamwise edge, leading edge, trailing edge, and spanwise edge (Watanabe et al. 2014*a*). The interface orientation is distinguished by using $\mathbf{n}$. Because $\mathbf{n}$ is the unit vector, it is represented by $(n_x, n_y, n_z) = (\cos\theta_x, \cos\theta_y, \cos\theta_z)$, where θ_x, θ_y, and θ_z are the angles between $\mathbf{n}$ and the x, y, and z directions, respectively. The cross-streamwise (spanwise) edge is the interface which faces in the $\pm y$ ($\pm z$) direction, and the leading (trailing) edge is the interface which faces in the x ($-x$) direction. Therefore, the interfaces at which $|n_y| > \cos 25°$, $n_x > \cos 25°$, $n_x < -\cos 25°$, and $|n_z| > \cos 25°$ are used as the cross-streamwise edge, the leading edge, the trailing edge, and the spanwise edge, respectively. The conditional statistics are calculated by using the interface detected in the region of $22 \le x/d \le 24$. Further detail on the calculation of the conditional statistics can be found in previous papers (Watanabe et al. 2014*c*, 2014*d*).

Figure 11 visualizes the T/NT interface (isosurface of $\phi/\langle\phi\rangle_{\rm C} = 0.1$). The interface appears for a wide range of the interface height $Y_{\rm I}$. The interface shows the convoluted structures, and is similar to the interface observed in the DNS of spatially developing planar jets (Watanabe et al. 2014*a*, 2014*d*, Wu et al. 2014).

Figure 12 shows the conditional mean scalar $\langle\phi\rangle_{\rm I}$ for $Sc = 1$. In the DNS of planar jets (Watanabe et al. 2014*b*), it was found that $\langle\phi\rangle_{\rm I}$ is small near the trailing edge compared with those near other two interfaces. This tendency can be observed in the ILES results. Similar to the conditional mean scalar profiles obtained by the

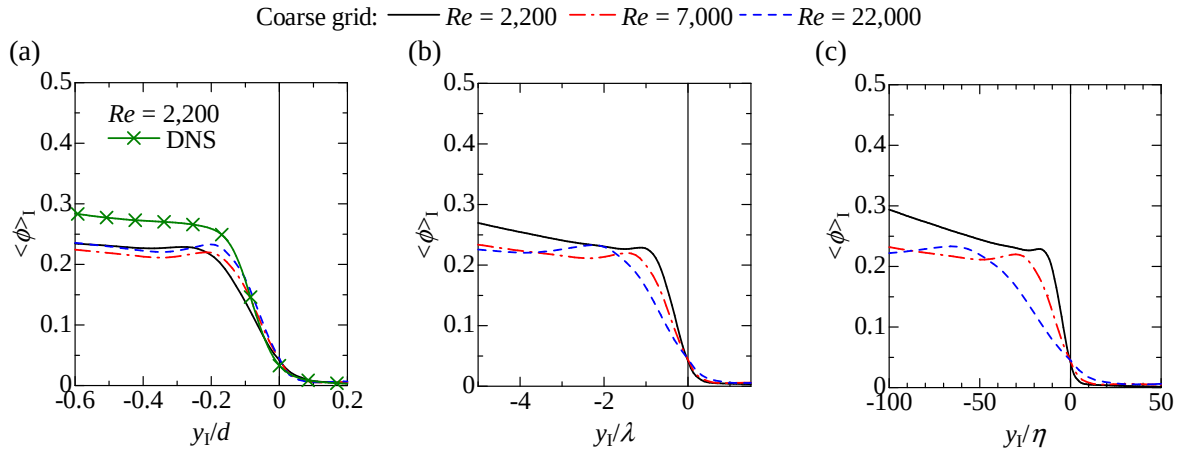

Figure 13. Conditional mean scalar near cross-streamwise at $x/d = 23$ obtained by the coarse-grid ILES. The distance from the T/NT interface is normalized by (a) width of the jet inlet d, (b) Taylor microscale $\lambda = (10\nu k/\epsilon)^{1/2}$, and (c) Kolmogorov lengthscale $\eta = (\nu^3/\epsilon)^{1/4}$. The Taylor microscale and Kolmogorov lengthscale are calculated on the jet centerline from ϵ in figure 8. The DNS result (Watanabe et al. 2014*d*) is shown in figure (a) for comparison.

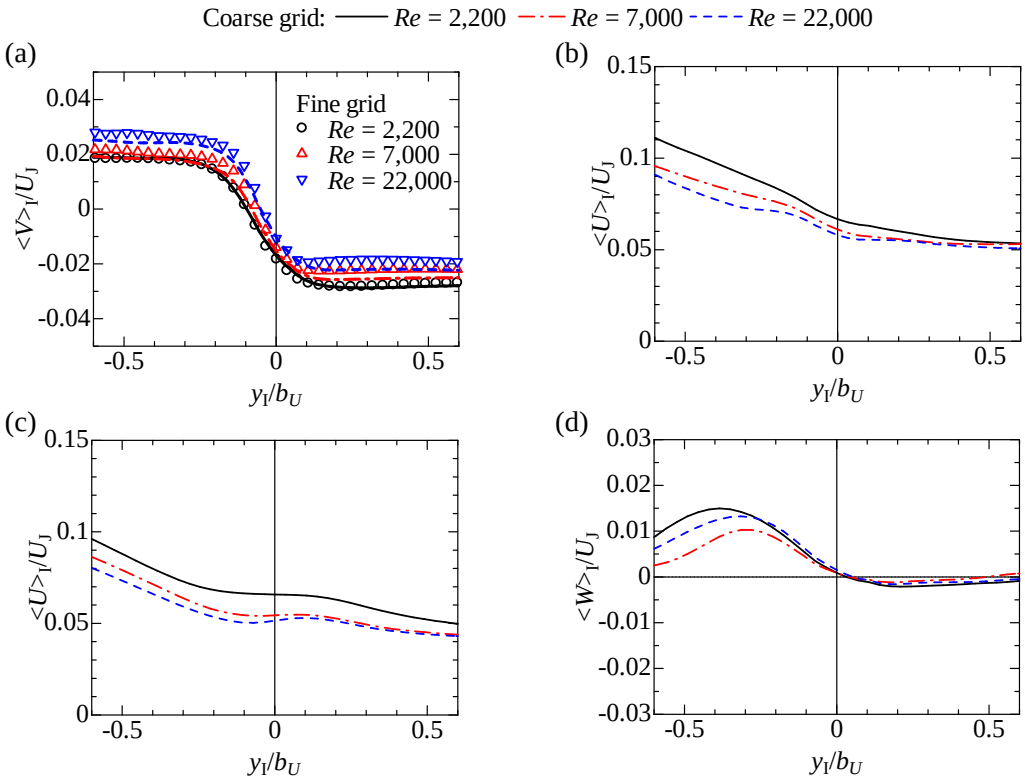

Figure 14. Conditional mean velocity normal to the interface at $x/d = 23$ obtained by the coarse-grid ILES: (a) cross-streamwise edge (lateral velocity V); (b) leading edge (streamwise velocity U); (c) trailing edge (U); (d) spanwise edge (spanwise velocity W). The results in the fine-grid ILES are also shown in figure(a).

DNS (Watanabe et al. 2014*a*, 2014*b*, Gampert et al. 2014*a*), $\langle\phi\rangle_{\mathrm{I}}$ in the ILES also shows a jump near the interface. The slope of the jump is slightly steeper for the fine-grid ILES especially for the high Re cases. Figure 13 shows $\langle\phi\rangle_{\mathrm{I}}$ against the distance from the T/NT interface normalized by the width of the jet inlet d, Taylor microscale $\lambda = (10\nu k/\epsilon)^{1/2}$, and Kolmogorov lengthscale $\eta = (\nu^3/\epsilon)^{1/4}$. The DNS result for $Re = 2,200$ (Watanabe et al. 2014*d*) is shown in figure (a) for comparison. The slope of the scalar jump across the T/NT interface is steeper in the DNS than in the ILES. Although the width of the jump is expected to scale with λ or η (da Silva et al. 2014), it scales with d in the ILES rather than λ or η. In the present simulations, the spatial resolutions relative to λ and η become worse as Re increases. Because the flow fields at small scales are not resolved in the LES, the interface thickness in the ILES is greatly affected by the computational grid sizes. The T/NT interface thickness in $\langle\phi\rangle_{\mathrm{I}}$ in the ILES is larger for the spanwise edge. In the coarse-grid ILES, the grid size in the z direction is 2.4 times larger than in the x direction. This larger grid in the z direction is related to the larger T/NT interface thickness for the spanwise edge in the ILES.

Figure 14 shows the conditional mean velocity in the interface normal direction. The interface normal components near the cross-streamwise edge and the leading and trailing edges are the lateral velocity V and streamwise velocity U, respectively. Here, negative V denotes the velocity toward the jet centerline. For the spanwise edge, the spanwise velocity W is the interface normal component, where positive W denotes the spanwise velocity toward the non-turbulent regions (positive y_{I} direction). Near the cross-streamwise edge, the movements of turbulent and non-turbulent fluids are opposite to each other in a mean sense because of outward spreading of turbulent fluids and inward motions in non-turbulent regions. Thus, the mean velocity near the cross-streamwise edge is toward the interface. The lateral velocity V at the cross-streamwise edge is related to the entrainment velocity, E_{B}, by $E_{\mathrm{B}} = -2\langle V\rangle_{\mathrm{I}}$ (Westerweel et al. 2009). From the conditional mean lateral velocity $\langle V\rangle_{\mathrm{I}}$ at the cross-streamwise edge, we can obtain $E_{\mathrm{B}}/U_{\mathrm{J}} = 0.036$, 0.032, and 0.023 for $Re = 2,200$, $7,000$, and $22,000$, respectively. When the Kolmogorov velocity $v_\eta = (\epsilon\nu)^{1/4}$ is used to normalize the entrainment velocity, $E_{\mathrm{B}}/v_\eta = 1.3$, 1.5, and 1.5, respectively, where v_η is calculated on the jet centerline from ϵ in figure 8. This Reynolds number dependence of E_{B} is found in the ILES results for both fine and coarse grids. Thus, as in the direct measurement of the entrainment velocity in previous experiments (Holzner & Lüthi 2011), the entrainment velocity estimated in the ILES also scales with the Kolmogorov velocity.

We can find the outward motion of the turbulent fluids near the spanwise edge as confirmed by positive $\langle W\rangle_{\mathrm{I}}$ in the turbulent regions. Near the leading and trailing edges, the turbulent fluid has a larger streamwise velocity than the non-turbulent one, and the difference in $\langle U\rangle_{\mathrm{I}}$ between the turbulent and non-turbulent regions is slightly small near the trailing edge. The turbulent fluids are located upstream and downstream of the leading and trailing edges, respectively. Therefore, $\langle U\rangle_{\mathrm{I}}$ shows that the velocity in the turbulent region is toward the interface near the leading edge, and the turbulent fluid approaches the leading edge. These conditional profiles of the velocity in the

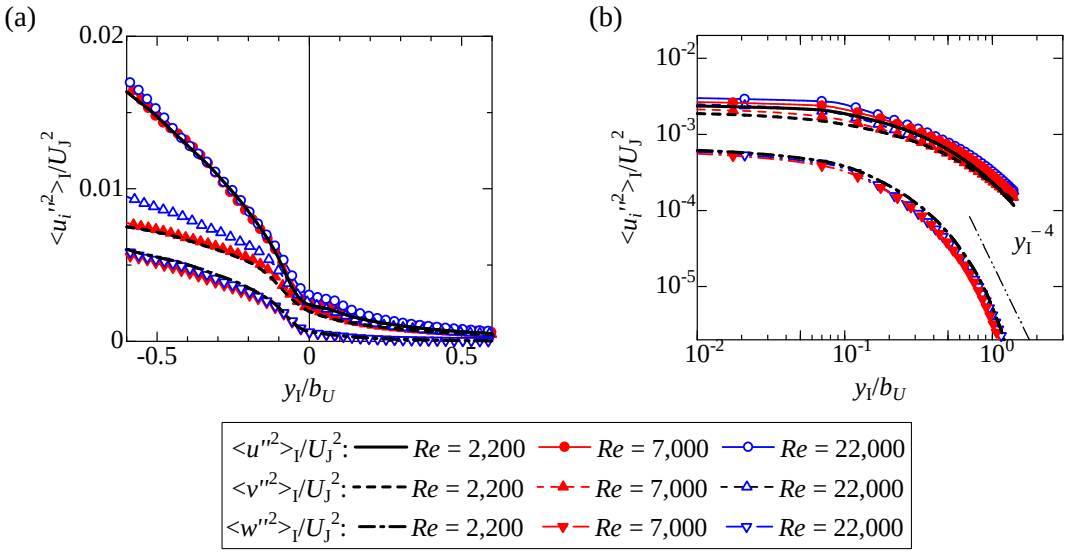

Figure 15. (a) Conditional velocity variance near cross-streamwise edge at $x/d = 30$. (b) Logarithmic plot of (a) in non-turbulent region.

interface normal direction agree with the DNS of a planar jet at $Re = 2,200$ (Watanabe et al. 2014*d*). It was found that the strain-field near the interface is strongly affected by the velocity relative to the interface movement in the interface normal direction (Watanabe et al. 2014*c*). Therefore, the relative velocity, which is greatly different near the trailing edge from the other interfaces, can cause the interface orientation dependence of the interface characteristics. Figure 14 shows that the large-scale velocity field near the interface is qualitatively independent of Re, indicating that the interface orientation dependence caused by the velocity field (Watanabe et al. 2014*c*) is similar between the low and high Re cases.

The conditional velocity variance $\langle u_i''^2 \rangle_{\rm I}$ is calculated from the velocity fluctuation from the conditional mean velocity $u_i'' \equiv U_i - \langle U_i \rangle_{\rm I}$. Figure 15(a) shows $\langle u_i''^2 \rangle_{\rm I}$ near the cross-streamwise edge. The profiles are almost independent of Re. The spanwise component $\langle w''^2 \rangle_{\rm I}$ is the smallest, in agreement with a temporally developing jet (Taveira & da Silva 2013). Even in the non-turbulent region, $\langle u_i''^2 \rangle_{\rm I}$ has a non-zero value, and decays in the $y_{\rm I}$ direction. Figure 15(b) shows a decay of $\langle u_i''^2 \rangle_{\rm I}$ in the $y_{\rm I}$ direction in the non-turbulent region. Phillips (1955) showed that in the non-turbulent region far away from the T/NT interface, $\langle u_i''^2 \rangle_{\rm I}$ decays as $\langle u_i''^2 \rangle_{\rm I} \sim y_{\rm I}^{-4}$. In figure 15(b), the decay of $\langle w''^2 \rangle_{\rm I}$ obeys this power low far away from the interface. However, the decay rate of $\langle u''^2 \rangle_{\rm I}$ and $\langle v''^2 \rangle_{\rm I}$ is smaller than the theoretical value. The profiles of $\langle u_i''^2 \rangle_{\rm I}$ suggest that a larger distance from the T/NT interface might be required for $\langle u''^2 \rangle_{\rm I}$ and $\langle v''^2 \rangle_{\rm I}$ to exhibit $\langle u_i''^2 \rangle_{\rm I} \sim y_{\rm I}^{-4}$.

4. Conclusion

Turbulent planar jets with passive scalar transports were simulated for various Reynolds and Schmidt numbers by the ILES using low-pass filtering as an implicit SGS model. We confirmed that the self-similar profiles of statistics obtained by the ILES are quite similar to the DNS and experimental results. The ILES data were used for investigating the budget of resolved turbulent kinetic energy k and scalar variance $\langle\phi'^2\rangle$ and the large-scale characteristics of velocity and scalar fields near the T/NT interface.

The transport equations of k and $\langle\phi'^2\rangle$ were explicitly evaluated from the ILES data except for the dissipation terms, which were obtained from the budget of k and $\langle\phi'^2\rangle$. The budget of k obtained by the ILES qualitatively agrees with the results of the DNS and experiments for both high and low Reynolds number cases. The mean scalar dissipation rate in the self-similar region is similar between the ILES and the DNS. These results showed that the ILES is a useful tool for investigating the transport mechanism of k and $\langle\phi'^2\rangle$, which are often important in modeling of turbulent flows. As predicted from the scaling argument, the ILES result shows that the mean dissipation rates of k decays according to $(x/d)^{-2.5}$ in the downstream region. However, for the decay of the mean scalar dissipation rate, the decay rate evaluated by the ILES is smaller than that theoretically predicted, but is close to the experimental results by Su & Clemens (1999). By using the mean dissipation rate of k and $\langle\phi'^2\rangle$, the mechanical-to-scalar timescale ratio C_ϕ was evaluated in the self-similar region of planar jets. For the high Re case, C_ϕ is close to the isotropic value ($C_\phi = 2$) near the jet centerline. However, when Re is not large, C_ϕ is smaller than 2 even near the jet centerline. The Sc dependence of C_ϕ was clearly observed only for the low Re case. Except for the outer edge of the jet, C_ϕ ranges from 1.0 to 2.0 depending on the lateral location and the Reynolds and Schmidt numbers. It should be noted the Reynolds number and Schmidt number effects obtained in the LES are partial because of indirect effects on the resolved quantities through the SGS stress and scalar flux.

The T/NT interface was investigated by using the scalar isosurface for $Sc = 1$. The conditional statistics were calculated conditioned on the distance from the interface for four interface orientations. The velocity and scalar fields near the interface depends on the interface orientation for all Re computed in the present ILES. Similar to the low Reynolds number case investigated by previous DNS (Watanabe et al. 2014*b*, 2014*c*), the velocity toward the interface is observed in the turbulent region except in the vicinity of the trailing edge in the planar jet at higher Reynolds numbers. The spanwise velocity fluctuations decays with y_{I}^{-4} (y_{I}: distance from the interface) in the non-turbulent region far away from the interface.

Acknowledgments

The authors acknowledge the anonymous referees for valuable comments. This work was supported by JSPS KAKENHI Grant Number 25002531 and MEXT KAKENHI

Grant Numbers 25289030, 25289031, and 25630052.

References

Bilger R W 2004 Some aspects of scalar dissipation *Flow, Turbul. Combust.* **72**, 93–114.

Bisset D K, Hunt J C R & Rogers M M 2002 The turbulent/non-turbulent interface bounding a far wake *J. Fluid Mech.* **451**, 383–410.

Bogey C & Bailly C 2004 A family of low dispersive and low dissipative explicit schemes for flow and noise computations *J. Comput. Phys.* **194**(1), 194–214.

Bogey C & Bailly C 2005 Decrease of the effective Reynolds number with eddy-viscosity subgrid modeling *AIAA J.* **43**(2), 437–439.

Bogey C & Bailly C 2006 Large eddy simulations of round free jets using explicit filtering with/without dynamic Smagorinsky model *Int. J. Heat Fluid Flow* **27**(4), 603–610.

Bogey C & Bailly C 2009 Turbulence and energy budget in a self-preserving round jet: direct evaluation using large eddy simulation *J. Fluid Mech.* **627**, 129–160.

Corrsin S 1951 The decay of isotropic temperature fluctuations in an isotropic turbulence *J. Aeronaut. Sci.* **18**, 417–423.

da Silva C B 2009 The behavior of subgrid-scale models near the turbulent/nonturbulent interface in jets *Phys. Fluids* **21**(8), 081702.

da Silva C B, Hunt J C R, Eames I & Westerweel J 2014 Interfacial layers between regions of different turbulence intensity *Annu. Rev. Fluid Mech.* **46**, 567–590.

da Silva C B, Lopes D C & Raman V 2015 The effect of subgrid-scale models on the entrainment of a passive scalar in a turbulent planar jet *J. Turbulence* **16**, 342–366.

da Silva C B & Pereira J C F 2008 Invariants of the velocity-gradient, rate-of-strain, and rate-of-rotation tensors across the turbulent/nonturbulent interface in jets *Phys. Fluids* **20**(5), 055101.

Dai Y, Kobayashi T & Taniguchi N 1994 Large eddy simulation of plane turbulent jet flow using a new outflow velocity boundary condition *JSME Int. J., Ser. B* **37**(2), 242–253.

Deo R C, Mi J & Nathan G J 2008 The influence of Reynolds number on a plane jet *Phys. Fluids* **20**(7), 075108.

Deo R C, Nathan G J & Mi J 2013 Similarity analysis of the momentum field of a subsonic, plane air jet with varying jet-exit and local Reynolds numbers *Phys. Fluids* **25**(1), 015115.

Fox R O 2003 *Computational Models for Turbulent Reacting Flows* Cambridge Univ. Pr.

Gampert M, Boschung J, Hennig F, Gauding M & Peters N 2014*a* The vorticity versus the scalar criterion for the detection of the turbulent/non-turbulent interface *J. Fluid Mech.* **750**, 578–596.

Gampert M, Kleinheinz K, Peters N & Pitsch H 2014*b* Experimental and numerical study of the scalar turbulent/non-turbulent interface layer in a jet flow *Flow, Turbul. Combust.* **92**(1-2), 429–449.

Germano M, Piomelli U, Moin P & Cabot W H 1991 A dynamic subgrid-scale eddy viscosity model *Phys. Fluids A* **3**(7), 1760–1765.

Gutmark E & Wygnanski I 1976 The planar turbulent jet *J. Fluid Mech.* **73**(03), 465–495.

Holzner M & Lüthi B 2011 Laminar superlayer at the turbulence boundary *Phys. Rev. Lett.* **106**, 134503.

Kempf A, Klein M & Janicka J 2005 Efficient generation of initial-and inflow-conditions for transient turbulent flows in arbitrary geometries *Flow, Turbul. Combust.* **74**(1), 67–84.

Klein M, Sadiki A & Janicka J 2003 Investigation of the influence of the Reynolds number on a plane jet using direct numerical simulation *Int. J. Heat Fluid Flow* **24**(6), 785–794.

Le Ribault C, Sarkar S & Stanley S A 1999 Large eddy simulation of a plane jet *Phys. Fluids* **11**(10), 3069–3083.

Lindstedt R P, Louloudi S A & Vaos E M 2000 Joint scalar probability density function modeling of pollutant formation in piloted turbulent jet diffusion flames with comprehensive chemistry *Proc. Combust. Inst.* **28**(1), 149–156.

Mathew J, Lechner R, Foysi H, Sesterhenn J & Friedrich R 2003 An explicit filtering method for large eddy simulation of compressible flows *Phys. Fluids* **15**(8), 2279–2289.

Mitarai S, Riley J J & Kosaly G 2005 Testing of mixing models for Monte Carlo probability density function simulations *Phys. Fluids* **17**(4), 047101.

Moin P, Squires K, Cabot W & Lee S 1991 A dynamic subgrid-scale model for compressible turbulence and scalar transport *Phys. Fluids A* **3**(11), 2746–2757.

Morinishi Y, Lund T S, Vasilyev O V & Moin P 1998 Fully conservative higher order finite difference schemes for incompressible flow *J. Comput. Phys.* **143**(1), 90–124.

Phillips O M 1955 The irrotational motion outside a free turbulent boundary *in* 'Proc. Cambridge Philos. Soc.' Vol. 51 Cambridge Univ. Press pp. 220–229.

Pope S B 1985 PDF methods for turbulent reactive flows *Prog. Energy Combust. Sci.* **11**(2), 119–192.

Schwertfirm F & Manhart M 2007 DNS of passive scalar transport in turbulent channel flow at high Schmidt numbers *Int. J. Heat Fluid Flow* **28**(6), 1204–1214.

Smagorinsky J 1963 General circulation experiments with the primitive equations: I. the basic experiment *Mon. Weather Rev.* **91**(3), 99–164.

Spalart P R, Moser R D & Rogers M M 1991 Spectral methods for the Navier-Stokes equations with one infinite and two periodic directions *J. Comput. Phys.* **96**(2), 297–324.

Stanley S A, Sarkar S & Mellado J P 2002 A study of the flow-field evolution and mixing in a planar turbulent jet using direct numerical simulation *J. Fluid Mech.* **450**, 377–407.

Stolz S & Adams N A 1999 An approximate deconvolution procedure for large-eddy simulation *Phys. Fluids* **11**(7), 1699–1701.

Stolz S, Adams N A & Kleiser L 2001*a* An approximate deconvolution model for large-eddy simulation with application to incompressible wall-bounded flows *Phys. Fluids* **13**(4), 997–1015.

Stolz S, Adams N A & Kleiser L 2001*b* The approximate deconvolution model for large-eddy simulations of compressible flows and its application to shock-turbulent-boundary-layer interaction *Phys. Fluids* **13**(10), 2985–3001.

Su L K & Clemens N T 1999 Planar measurements of the full three-dimensional scalar dissipation rate in gas-phase turbulent flows *Exp. Fluids* **27**(6), 507–521.

Suresh P R, Srinivasan K, Sundararajan T & Das S K 2008 Reynolds number dependence of plane jet development in the transitional regime *Phys. Fluids* **20**(4), 044105.

Taveira R R & da Silva C B 2013 Kinetic energy budgets near the turbulent/nonturbulent interface in jets *Phys. Fluids* **25**, 015114.

Taveira R R, Diogo J S, Lopes D C & da Silva C B 2013 Lagrangian statistics across the turbulent-nonturbulent interface in a turbulent plane jet *Phys. Rev. E* **88**(4), 043001.

Terashima O, Sakai Y & Nagata K 2012 Simultaneous measurement of velocity and pressure in a plane jet *Exp. Fluids* **53**(4), 1149–1164.

Terashima O, Sakai Y & Nagata K 2014 Simultaneous measurement of all three velocity components and pressure in a plane jet *Meas. Sci. Technol.* **25**(5), 055301.

Watanabe T, Sakai Y, Nagata K, Ito Y & Hayase T 2014*a* Enstrophy and passive scalar transport near the turbulent/non-turbulent interface in a turbulent planar jet flow *Phys. Fluids* **26**(10), 105103.

Watanabe T, Sakai Y, Nagata K, Ito Y & Hayase T 2014*b* Reactive scalar field near the turbulent/non-turbulent interface in a planar jet with a second-order chemical reaction *Phys. Fluids* **26**(10), 105111.

Watanabe T, Sakai Y, Nagata K, Ito Y & Hayase T 2014*c* Vortex stretching and compression near the turbulent/nonturbulent interface in a planar jet *J. Fluid Mech.* **758**, 754–785.

Watanabe T, Sakai Y, Nagata K, Ito Y & Hayase T 2014*d* Wavelet analysis of coherent vorticity near the turbulent/non-turbulent interface in a turbulent planar jet *Phys. Fluids* **26**(9), 095105.

Watanabe T, Sakai Y, Nagata K & Terashima O 2014*e* Experimental study on the reaction rate of a second-order chemical reaction in a planar liquid jet *AIChE J.* **60**(11), 3969–3988.

Watanabe T, Sakai Y, Nagata K, Terashima O & Kubo T 2012 Simultaneous measurements of reactive scalar and velocity in a planar liquid jet with a second-order chemical reaction *Exp. Fluids*

53(5), 1369–1383.

Westerweel J, Fukushima C, Pedersen J M & Hunt J C R 2005 Mechanics of the turbulent-nonturbulent interface of a jet *Phys. Rev. Lett.* **95**(17), 174501.

Westerweel J, Fukushima C, Pedersen J M & Hunt J C R 2009 Momentum and scalar transport at the turbulent/non-turbulent interface of a jet *J. Fluid Mech.* **631**, 199–230.

Wu N, Sakai Y, Nagata K, Suzuki H, Terashima O & Hayase T 2013 Analysis of flow characteristics of turbulent plane jets based on velocity and scalar fields using DNS *J. Fluid Sci. Tech.* **8**(3), 247–261.

Wu N, Sakai Y, Nagata K, Ito Y, Terashima O & Hayase T 2014 Influence of Reynolds number on coherent structure, flow transition, and evolution of the plane jet *J. Fluid Sci. Tech.* **9**(2), JFST0013.

Xu J & Pope S B 2000 PDF calculations of turbulent nonpremixed flames with local extinction *Combust. Flame* **123**(3), 281–307.